Heliyon 10 (2024) e38854

Contents lists available at ScienceDirect

Heliyon

journal homepage: www.cell.com/heliyon

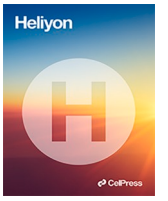

Research article

Molecular dynamics study of mechanical stability of Ti_4C_3 MXene subjected to chirality, temperature, strain rate, and point-vacancy for Lithium-ion batteries

Wahidur Rahman Sajal, Md. Mehidi Hassan, Jahirul Islam *, Tipu Sultan, Md. Bokhtiar Hossen, Abdullah Arafat

Department of Materials Science and Engineering, Khulna University of Engineering & Technology, Khulna-9203, Bangladesh

ARTICLE INFO

Keywords:
Molecular dynamics
MXene
Mechanical behavior
Temperature effect
Vacancy effect

ABSTRACT

Two-dimensional Ti_4C_3 MXene has recently emerged as a promising electrode for Lithium-ion batteries (LIBs) because of its outstanding ion-transport abilities and high Li-absorbability. This study employed molecular dynamics simulation to explore the mechanical stability of Ti_4C_3 MXene subjected to various temperatures, strain rates, and vacancy concentrations. A slightly superior tensile strength and elasticity modulus have been observed along zigzag directions, measuring 148.14 GPa and 29.17 GPa, respectively. On the other hand, armchair-oriented Ti_4C_3 MXene shows a considerably greater fracture strain of 0.259 due to its strain-hardening tendency at lower temperatures. Elevated temperature decreases both fracture strength and fracture strain, which is opposite to the effect of strain rate. Armchair loading has been revealed to be more sensitive to strain rate than its counter direction. Unlike temperature and strain rate, point vacancy significantly deteriorates the elastic modulus of Ti_4C_3 MXene. Carbon vacancies are more probable than titanium vacancies, which have less formation energy. The atomistic deformation profile supports the predicted values of fracture strain from stress-strain behavior. This in-depth study offers a detailed understanding of the mechanical behavior of Ti_4C_3 MXene under diverse circumstances, which will aid further experimental study and be beneficial for adopting Ti_4C_3 as anode materials in LIBs.

1. Introduction

Humankind's future on earth and its increasing economic prosperity largely depend on our ability to sustainably utilize the remaining fossil fuel to produce sophisticated energy harvesting technologies [1]. The ever-increasing popularity of portable electronics has increased the prominence of storing energy efficiently [2]. Efficient energy storage and conversion technologies, in turn, demand the advanced development of highly effective electrode materials and electrocatalysts [3]. Li-ion batteries (LIBs) are considered one of the most popular portable energy devices due to their higher energy density, long shelf life, and reasonable cost [4, 5]. The functionality of LIBs is highly dependent on the efficiency, specific capacity, and mechanical stability of the electrode material [6–8]. Numerous studies have been conducted in recent years in search of credible anode materials for LIBs, and given their intrinsic physical and electrochemical attributes, two-dimensional (2D) nanomaterials have emerged as the most promising alternatives [9–11].

* Corresponding author.
E-mail address: jahirul@mse.kuet.ac.bd (J. Islam).

https://doi.org/10.1016/j.heliyon.2024.e38854
Received 16 April 2024; Received in revised form 3 September 2024; Accepted 1 October 2024
Available online 2 October 2024
2405-8440/© 2024 The Authors. Published by Elsevier Ltd. This is an open access article under the CC BY-NC-ND license (http://creativecommons.org/licenses/by-nc-nd/4.0/).

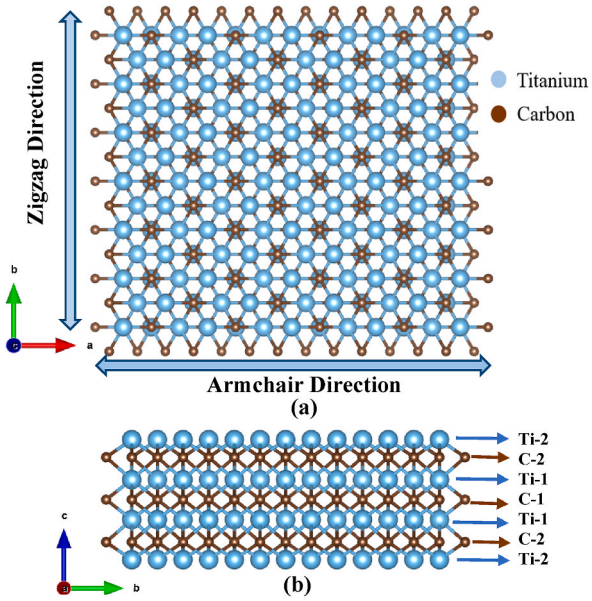

Fig. 1. Atomic structure - (a) XY plane view, and (b) side view of the developed structure of Ti_4C_3.

Graphene, primarily used in 2D materials, has been observed to possess excellent conductivity and structural stability as an anode material. However, its poor ion transfer rate, low volumetric density, and safety concerns undermine its commercialization [10].

In recent years, several researchers have focused on newly invented two-dimensional transition metal carbides and nitrides called MXenes and their derivatives. The chemical formula of MXenes is $M_{n+1}X_{n,}$ and its derivative is expressed as $M_{n+1}X_nT_x$, where M is a transition metal (such as Ti, Nb, V, or Ta), X stands for either C or N, and T denotes the surface terminator (O, H, F or OH) [12–14]. MXenes are synthesized from their three-dimensional (3D) counterpart, known as MAX phases (A is a group IIIA or IVA element), by etching out the A elements [15]. In recent years, MXenes have been the subject of several experimental as well as theoretical studies, and it has been reported that they offer ground-breaking prospects to be employed as anode materials in LIBs and other electrochemical devices owing to their unique structural and electrochemical properties [16–18]. Due to its exceptional structural flexibility, high charge densities, excellent reversibility, and ability to withstand prolonged cycle life, $Ti_{n+1}C_n$ (n = 1,2,3) MXenes is the most promising anode material [19,20].

Since it is nearly impossible to experimentally characterize the mechanical properties of exceptionally thin MXenes sheets, most works on their characterization are based on computational methods [13]. Utilizing molecular dynamics investigation, Borysiuk et al. calculated the bending rigidity of all the $Ti_{n+1}C_n$ MXenes and revealed outstanding bending qualities comparable to graphene and MoS_2 [21]. According to a recent study based on DFT, the elastic constants of Ti_2C, Ti_3C_2, and Ti_4C_3 were anticipated to be 636 GPa, 523 GPa, and 512 GPa, respectively [22]. With a third-generation COMB potential and classical molecular dynamics simulation, Hatam-Lee et al. [23,24] implemented a more reasonable approach to investigate the elastic properties of titanium carbide and nitride MXenes. In the armchair and zigzag loading directions, the estimated elastic modulus of Ti_2C was 203 GPa and 207 GPa, respectively. Elastic modulus values for Ti_3C_2 were reported to be lower than those for Ti_2C, measuring 130 and 135 GPa in the armchair and zigzag directions, respectively. With increasing MXene's thickness, a decreasing trend in the elastic modulus of $Ti_{n+1}C_n$ MXene has also been reported [23].

Recent first-principles computations by Huang et al. [25] revealed that Ti_4C_3 MXene possesses excellent electron transport properties, high Li-ion absorbing abilities, and good thermal stability to be fitted as a high-quality anode for LIBs. However, the mechanical stability of Ti_4C_3 MXene in various environmental circumstances inside the battery cells is still to be ensured when designing anode materials for practical implementations. Temperature, loading rates, loading directions, and vacancy concentrations have all been found to profoundly affect the mechanical behavior of layered 2D systems [26–28]. It has been reported that elevated temperature has a detrimental effect on the mechanical performance of monolayer systems, resulting from thermal vibration, which causes a declining trend in tensile strength [29]. Contrary to temperature, increases in strain rates have been found to increase the structure's fracture strength and failure strain [30]. Along with temperatures and strain rates, mechanical properties have also been affected by various structural defects [31,32]. Different kinds of defects, including point vacancies and edge defects, are inevitable in manufacturing nanosheets from their ternary counterpart [27,33]. Hence, several studies have been carried out in recent years to explore the influence of various types of defects on the tensile mechanical characteristics of 2D monolayers, including graphene [33], MoS_2 [34], and Ti_3C_2 MXene [35]. According to reports, vacancies and imperfections profoundly decrease the monolayers' fracture strength, strain, and even elastic modulus. Therefore, investigations into the mechanical properties of layered systems that consider all of these factors—temperature, strain rate, and vacancies—are of the utmost importance.

This study aims to implement classical molecular dynamics simulation to comprehensively and systematically evaluate how the

temperature, applied loading rates, loading orientations, and concentration of point vacancies would affect the mechanical characteristics of Ti_4C_3 MXene. We applied uniaxial strain and computed the modulus of elasticity, tensile strength, and fracture strain of the Ti_4C_3 MXene using the large-scale simulation software LAMMPS [36]. Developed structures were simulated at different temperatures ranging from 100 K to 900 K and strain rates from 0.0001 ps^{-1} to 0.0125 ps^{-1} to investigate the effects of temperature and strain rates. The radial distribution function (RDF) at various temperatures was utilized to understand the structural stability of the MXene sample. Strain rate sensitivity was investigated to determine the significance of applied loading rates on the tensile-mechanical behaviors of the Ti_4C_3 MXene. The detrimental influence of Ti and C point vacancies has also been extensively explored, taking vacancy concentrations ranging from 0.5 % to 3 %. The cohesive energy was approximated for each atom of the sample to qualitatively comprehend the influence of two types of point vacancies on the mechanical characteristics of Ti_4C_3 samples. The visualization software was also utilized to demonstrate how the fracture mechanism altered regarding loading direction, temperature, and induced vacancy concentration.

2. Computational details

In this study, atomistic Molecular Dynamics (MD) simulation tool LAMMPS was used to analyze the mechanical properties of Ti_4C_3 MXene and the effects of temperature, strain rates, loading directions, and point vacancies on its behavior. The Ti_4C_3 structure employed to simulate this study was computationally prepared by eliminating the Al atoms from its ternary MAX phase, Ti_4AlC_3. The atomic configuration of the prepared nanostructure is given in Fig. 1. The developed structure of Ti_4C_3 has a dimension of 8.54 nm by 7.4 nm along the XY plane and contains 5376 atoms. Seven atomic layers comprise the structure, four of which are made of titanium and three of carbon, as shown in Fig. 1(b). It is also apparent from the illustration in Fig. 1 that both Ti and C atoms in the structure have a coordination number of 6, except in the top and bottom layers. Depending on its synthesizing environment, top and bottom-layered Ti atoms can be bonded with appropriate surface terminators. However, this study utilized only the bare Ti_4C_3 MXene structure since it is chemically stable because its cohesive energy is lower than the corresponding MAX phase [37–39].

Empirically generated interatomic potentials play a crucial role in MD simulations for consistently and accurately predicting system behavior. Our simulated compound Ti_4C_3 has three possible interatomic interactions: Ti-Ti, Ti-C, and C-C. The optimized Tersoff potential, which has been found to replicate interatomic interactions and subsequent mechanical properties of many 2D monolayer systems, including graphene and h-BCN, was implemented in this study to describe all three interatomic interactions in the nanosheets [40,41]. Of late, an optimized bond order potential was developed for the hexagonal MAX phase of Ti_3C_2 MXene [42], which was found to replicate the interatomic interactions in layered hexagonal structures, including Ti_2C and Ti_3C_2 MXene as well. The calculated cohesive energy of Ti_4C_3 MXene utilizing this potential was also found to be closely fitted with both MD [43] and DFT-based computations [37,43]. Therefore, this bond order potential [42] was used for this study to describe the interactions between Ti-Ti, Ti-C, and C-C. According to this bond order potential, the total energy of the system, E, can be denoted as a function of r_{ij}, which represents the distance between two atoms, i and j.

$$E=\frac{1}{2}\sum_{i}\sum_{i\neq j}f_C(r_{ij})\left[f_R(r_{ij})+b_{ij}f_A(r_{ij})\right] \tag{1}$$

In Eq. (1), b_{ij} indicates the many-body bound function, which combines the coordination number with the bond strength and incorporates the bond's angular phenomena; f_A is the attractive and f_R is the repulsive portions of the corresponding interatomic interaction. The cutoff function is given as f_C, restricts interaction to a certain distance in order to reduce computing time as well as costs. The cutoff function is described as the following equation:

$$f_C(r_{ij})=\begin{cases}1 & r_{ij}<R-D\\ \frac{1}{2}-\frac{1}{2}\sin\left[\frac{\pi}{2}\frac{(r_{ij}-R)}{D}\right], & R-D<r_{ij}<R+D\\ 0 & r_{ij}>R+D\end{cases}, \tag{2}$$

In Eq. 2, R and D are typically defined so that only neighboring atoms within a specific range are included. Four free parameters- A, B, λ_1 and λ_2 are used in the employed bond-order potential as a form of Morse potential to approximate the two-body attractive and repulsive interactions for Ti-Ti, C-C, and Ti-C.

$$f_R(r_{ij})=A.\exp(-\lambda_1 r_{ij}), \tag{3}$$

$$f_A(r_{ij})=-B.\exp(-\lambda_2 r_{ij}), \tag{4}$$

Moreover, the bound function is approximated as:

$$b_{ij}=(1+\xi_{ij})^{-\frac{1}{2}}, \tag{5}$$

$$\xi_{ij}=\sum_{k\neq i,j}f_C(r_{ik})g(\theta_{ijk})\exp\left[\lambda_3(r_{ij}-r_{ik})\right], \tag{6}$$

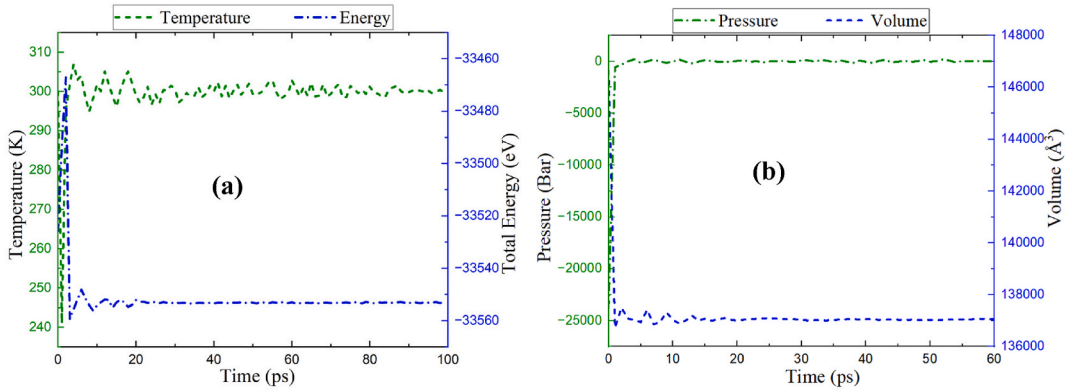

Fig. 2. Equilibration of (a) temperature and energy, and (b) volume and pressure of the Ti_4C_3 nanosheet as a function of time.

$$g(\theta_{ijk}) = \gamma\left(1 + \frac{c_i^2}{d_i^2} - \frac{c_i^2}{\left[d_i^2 + \left(\cos\theta_{ijk} - h_i\right)^2\right]}\right), \tag{7}$$

ξ_{ij} is approximated using a free parameter, λ_3 which is the only three body terms associated with the bond lengths. θ_{ijk} is used to approximate bond angles, which include four free parameters denoted as γ, c, d, and h. Since this bond order potential incorporates two-body and many-body interactions, it enhances the possibility of correctly emulating bond stretching and breaking bonds. To describe each interaction between Ti-Ti and C-C in the MXene, 11 free parameters were utilized, whereas 14 parameters were required to describe Ti-C interactions. 36 free parameters were used to describe all of the interactions in Ti_4C_3 MXene.

For the uniaxial tensile loading, periodic boundary conditions were applied in the X, Y, and Z directions. Although the simulation employed only 7.2 Å thick monolayers of Ti_4C_3, an 8 Å vacuum layer along both sides of the Z direction was taken into account to prevent atomic interactions in this direction. At various temperatures and strain rates, the velocity Verlet algorithm was employed to integrate the equations of motions to generate system evolutions. The system was allowed to equilibrate for a suitable number of MD timesteps at 300K with a time step of 0.001 ps at the beginning of the simulation. Canonical (NVT) ensembles were applied for 100 ps in conjunction with the conjugate gradient (CG) minimization method to minimize the system's energy. Once total energy had dropped to its minimum, an isothermal-isobaric (NPT) ensemble was employed to stabilize the volume and pressure for an additional 80 ps.

Tensile loading with a constant strain rate of 0.001 ps^{-1} was applied when the system reached equilibrium and thermodynamical parameters were steady. Tensile loading can be implemented in MD simulations using several methods [44,45]. The work adopted uniaxial tensile loading, which applies a constant loading rate across two opposing directions. The tensile properties of Ti_4C_3 systems were examined utilizing the resulting stress from the virial theorem [46]:

$$\sigma_{ij} = \frac{1}{V}\sum_{\beta=1}^{N} r_{\alpha\beta}^{i} f_{\alpha\beta}^{j} - m^{\alpha} v_i^{\alpha} v_j^{\alpha} \tag{8}$$

In Eq. 8, *ij* stands for Cartesian coordinates, atom indexes are denoted as α and β, whereas $r_{\alpha\beta}^{i}$ is the interatomic distance of the corresponding atoms. Interatomic force is indicated as $f_{\alpha\beta}^{j}$, m is atomic mass, and the volume of the considered simulation box is V. To determine the effects of different chiral directions, temperatures, strain rates, and point vacancies, the developed MXene samples were simulated repeatedly, adopting specific parameters. Finally, the deformation profile and bond breakage were depicted using a visualization package OVITO [47].

3. Results and discussion

3.1. Equilibration results

At the start of the simulation, the nanosheets were brought into equilibrium by employing the optimization procedures of two ensembles, NVT and NPT ensembles. At first, the system's total energy was minimized to 100 ps, combining the NVT ensemble with the CG energy minimization approach. The temperature, which is closely associated with kinetic energy, also stabilizes in tandem with the stabilization of the overall energy. Fig. 2(a) demonstrates the minimization of the system's total energy with time. After several ups and downs, the system's temperature relaxed to 300 K. In addition, the temperature took 90 ps to stabilize at 300 K, although the total energy of the system reached its minimum value at around 22 ps. Similarly, all the systems were relaxed at their intended temperature before being placed under strain. Once the temperature had stabilized, the pressure and volume of the system were equilibrated employing the NPT ensemble, as illustrated in Fig. 2(b). Unlike temperature, volume and pressure relaxed quite fast. However, the system was relaxed for 60 ps to achieve complete equilibrium. The system's equilibrated pressure was 0 Bar, as shown in Fig. 2(b), and

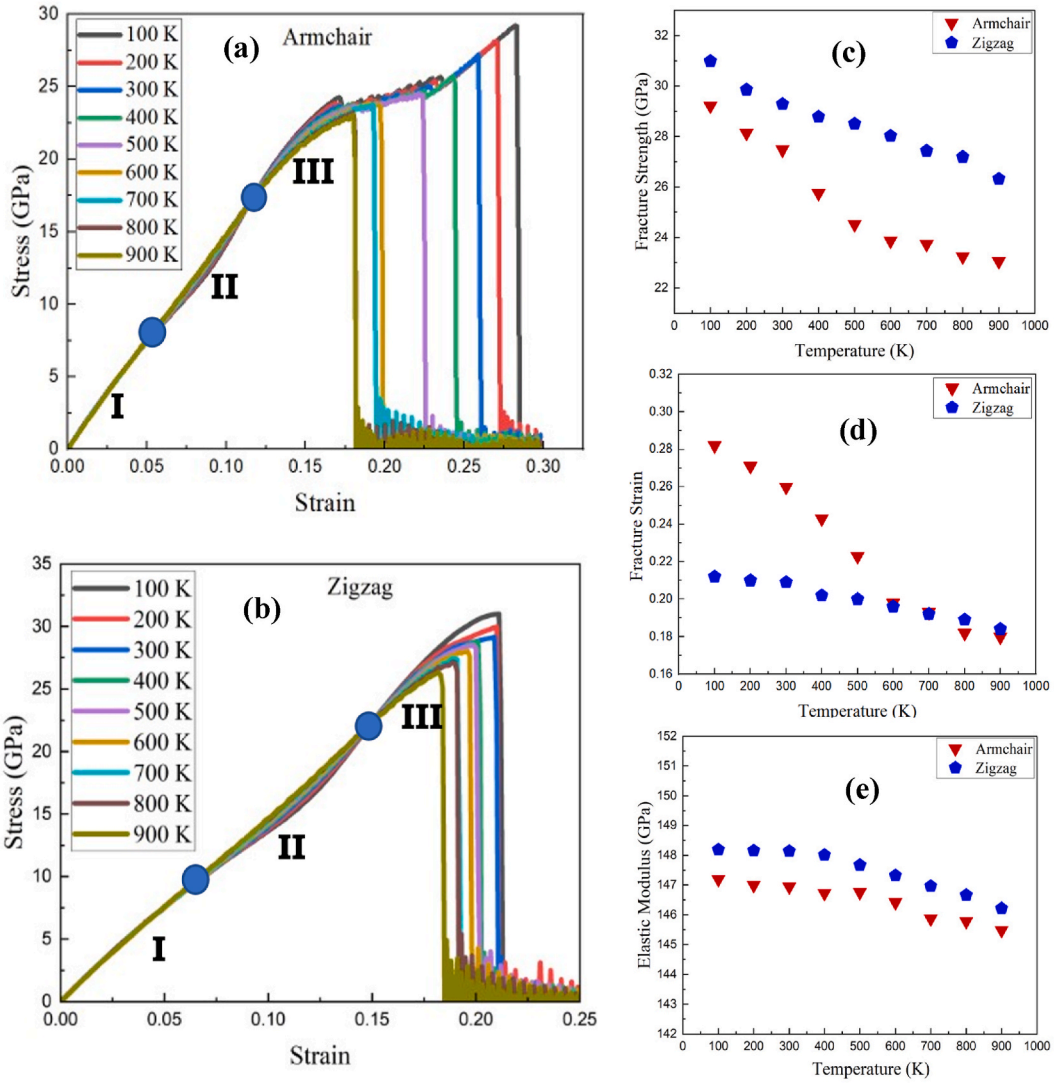

Fig. 3. Effect of temperature on stress-strain behavior of Ti_4C_3 nanosheet depending on (a) armchair loading and (b) zigzag loading direction, and resulting variations of the (c) fracture strength, (d) strain and (e) modulus of elasticity with temperature.

this value was maintained for all simulated systems. Because there is more negative potential energy than positive kinetic energy, the total energy of all the systems is eventually minimized to a negative value.

3.2. *Effect of temperature*

In order to use Li-ion batteries safely, proper control of the operating temperature is crucial, and the thermal stability of the electrode and separator at the intended temperature range must be guaranteed [48,49]. Therefore, investigating the electrode material's temperature-dependent mechanical behavior and thermal stability plays a significant role in designing LIBs. In this section, we examined the mechanical behavior of Ti_4C_3 MXene, simulating under various temperature conditions ranging from 100 K to 900 K with an increment of 100 K at the constant strain rate of 0.001 ps^{-1}. Once the system had reached absolute equilibrium, the uniaxial tensile strain was applied along armchair and zigzag orientations, and the consequent stress-strain response is presented in Fig. 3(a and b). However, the obtained stress-strain curves are unusual, unlike typical stress-strain behavior, they show three different regions before breaking down marked as I, II, and III in the curve. Especially this untypical stress-strain behavior is more prominent up to 500 K. For instance, the first part, which is up to the strain value of 0.07 and 0.08 in armchair and zigzag respectively, is completely linear due to the uniform bond elongation. The second part is observed in the strain range of 0.07–0.125 in the armchair and 0.08 to 0.15 in the zigzag direction, where there is a region of non-linear elasticity due to the conjugate influence of bond angle variation and bond elongation. After that, a second liner portion is observed which is known as 'second linearly elastic deformation (SLED)' [30]. This phenomenon is observed due to the applied cut-off distance in the potential and phase transformations as previously reported in 2D

Table 1
Calculated Young's modulus, tensile strength, and fracture strain of Ti_4C_3 at 300 K.

Property	Armchair Loading	Zigzag Loading
Young's Modulus (GPa)	146.94	148.14
Fracture Strength (GPa)	27.27	29.17
Fracture Strain	0.259	0.209

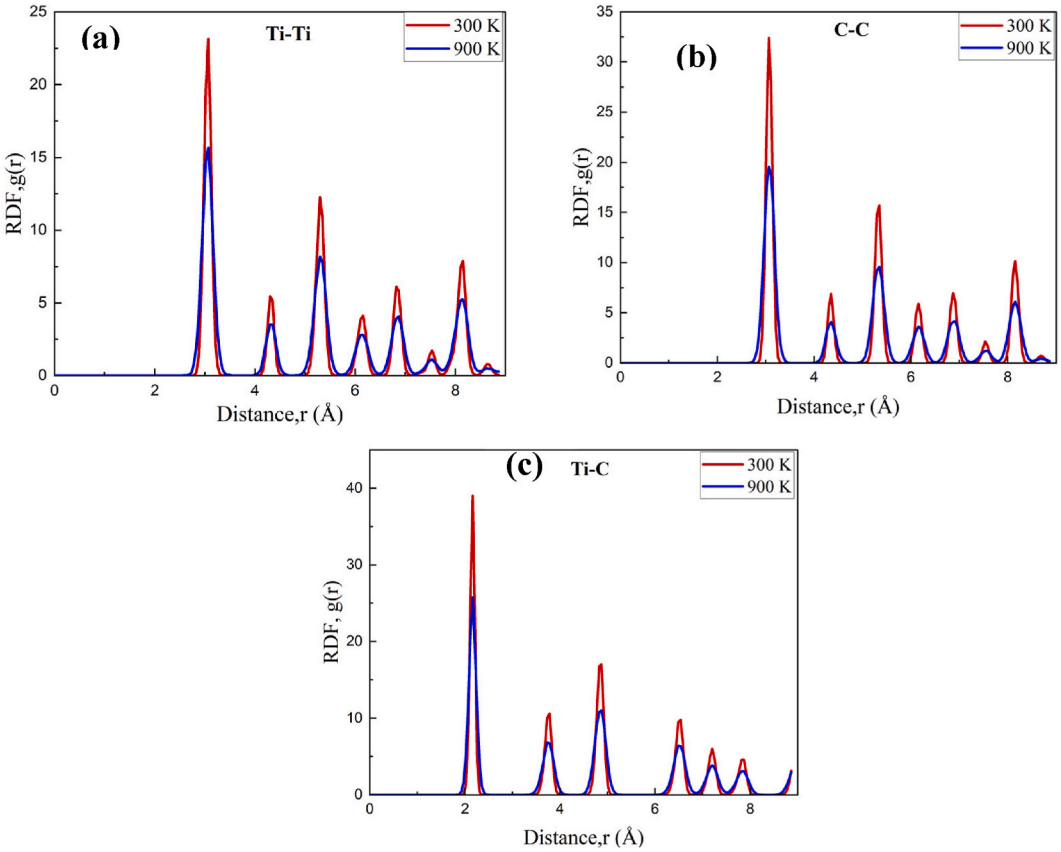

Fig. 4. Partial RDF of the nearest nighbours (a) Ti-Ti, (b) C-C, and (c) Ti-C of Ti_4C_3 MXene with increasing temperature.

SiGe [30], Ti_2C MXene [50], Ti_3C_2 MXene [35], and h-BN [51]. Thus, it appears that the phase transition and cut-off distance in the potential may be the source of this inconsistent stress-strain behavior.

To evaluate the mechanical performance of the Ti_4C_3 MXene in natural environmental conditions, we have taken the values of Young's modulus, fracture strength, and fracture strain from the stress-strain curve at 300 K, as shown in Table 1. At 300 K, the Ti_4C_3 structure orientated in the zigzag direction exhibits a comparatively better elastic modulus and fracture strength than armchair-oriented. The armchair-directed structure's elastic modulus and fracture strength are 146.94 GPa and 27.27 GPa, respectively, while the zigzag-directed structure displays the corresponding values of 148.14 GPa and 29.17 GPa. Elastic modulus and fracture strength are 0.82 % and 6.51 %, respectively, higher in the zigzag direction than in the armchair direction. On the other hand, the armchair-oriented nanosheet can sustain substantially higher strain before failing, measuring 0.259, which is 19.31 % greater than its counter orientation. As illustrated in Fig. 3(a and b), every strain-stress curve in the armchair and zigzag-directed loading have the same patterns, with an initial linear section demonstrating the presence of elasticity. The stress grows in proportion to the applied strain till the yield point is reached. The yield point was achieved immediately after the linear region along the zigzag direction—however, the armchair-directed samples at 100–500 K show substantial strain hardening before failing.

Fig. 3(c–e) shows the resulting values of fracture strength, fracture strain, and elastic modulus of Ti_4C_3 nanosheet with increasing temperature. It is evident from the plot that rising temperatures cause fracture strength and strain to decline. Higher temperatures produce thermal trembling inside nanosheets, reducing the bonds' rigidity and corresponding nanosheets. Resultingly, chemical bonds between atoms may rupture at a lesser value of stress, causing a reduction in fracture strength and fracture strain. Maximum fracture strength was obtained for the minimum value of temperature 100 K, measuring 29.21 GPa and 30.98 GPa, respectively, across armchair and zigzag directions. However, with increasing temperature from 100 K to 900 K, fracture strength reduces by about 21.08

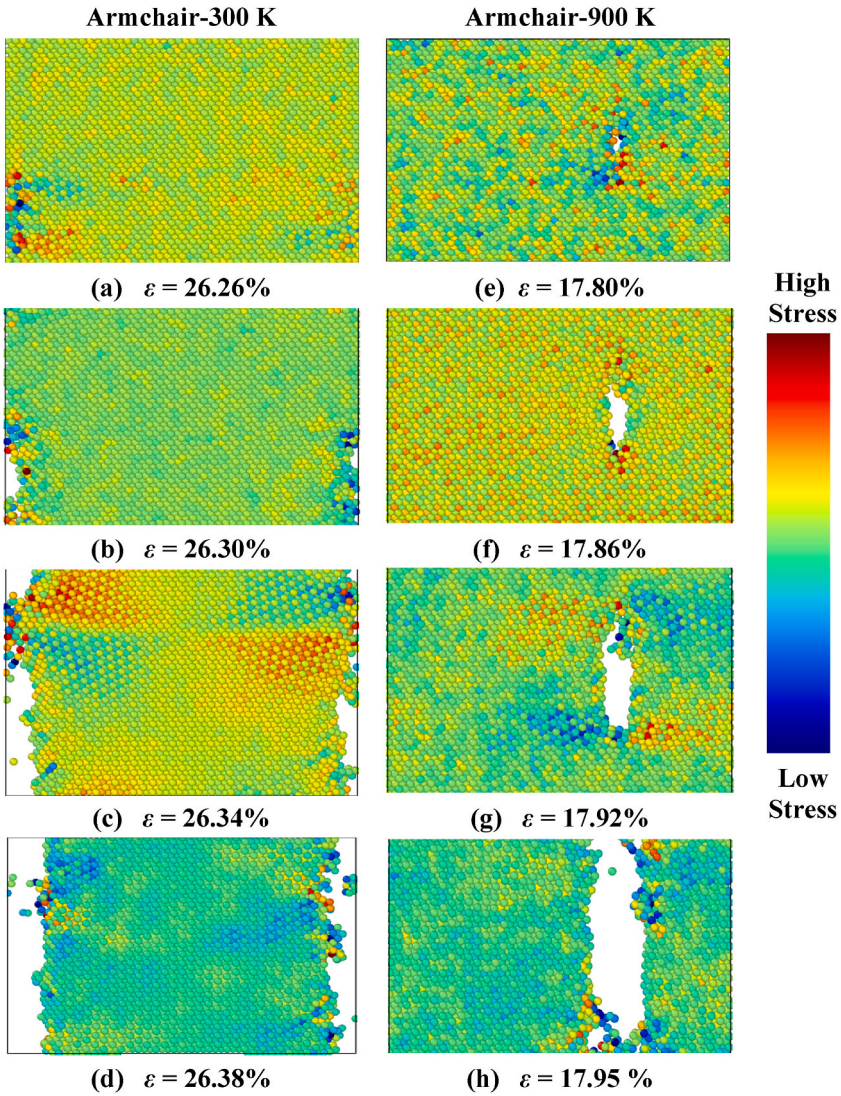

Fig. 5. Atomistic deformation profile of Ti_4C_3 nanosheets with increasing strain along armchair direction at temperature of (a–d) 300 K, and (e–h) 900 K.

% and 15.07 %, respectively, to reach 23.05 GPa and 26.31 GPa. Unlike fracture strength, fracture strain values at the lowest simulated temperature of 100 K are substantially more remarkable in the armchair direction than in the zigzag, as shown in Fig. 3(d). Armchair-oriented Ti_4C_3 nanosheet can withstand the highest fracture strain of 0.282 at 100 K, 24.82 % higher than the fracture strain of 0.212 in the zigzag-directed sample. The atomic arrangement of the Ti_4C_3 MXene sample shown in Fig. 1 can explain this unusual strain-taking ability in an armchair orientation. Following the atomic structure, each cell of the MXene structure contains four parallel bonds out of the 12 strain-carrying bonds along the armchair direction. Contrarily, the zigzag orientation has eight strain-carrying bonds, reducing the nanosheet's capability to carry strain along this orientation. The stress-strain diagram in Fig. 3(a, b) demonstrates that a significant strain hardening occurs after the linear elastic period at lower temperatures for armchair loading, whereas this does not happen for zigzag loading. For armchair and zigzag loading, fracture strain decreases by about 36.17 % and 13.20 %, respectively, with increasing temperatures from 100 K to 900 K. The considerable drops in the armchair direction due to the tendency of the strain hardening gradually diminish with temperature and are not observed beyond 500 K.

To examine the effect of temperature on the elastic modulus of Ti_4C_3 MXene, the values of elastic modulus were determined from the linear fit of the stress-strain diagram shown in Fig. 3(e). The linear fitting was performed for the entire elastic region up to the yield point in each of the stress-strain curves, following the approach used in previous studies [30,35]. As illustrated, the elastic modulus of Ti_4C_3 MXene is not significantly affected by temperature in the range of 100 K–900 K, changing by 1.16 % and 1.32 % in the armchair and zigzag directions, respectively. The stress-strain diagram in Fig. 3(a and b) also demonstrates that temperature has a negligible effect on elastic modulus because all of the curves' initial linear sections align up. According to the investigation, temperature significantly affects the Ti_4C_3 nanosheets' fracture strength and strain, but the elastic modulus is almost unaffected. The obtained

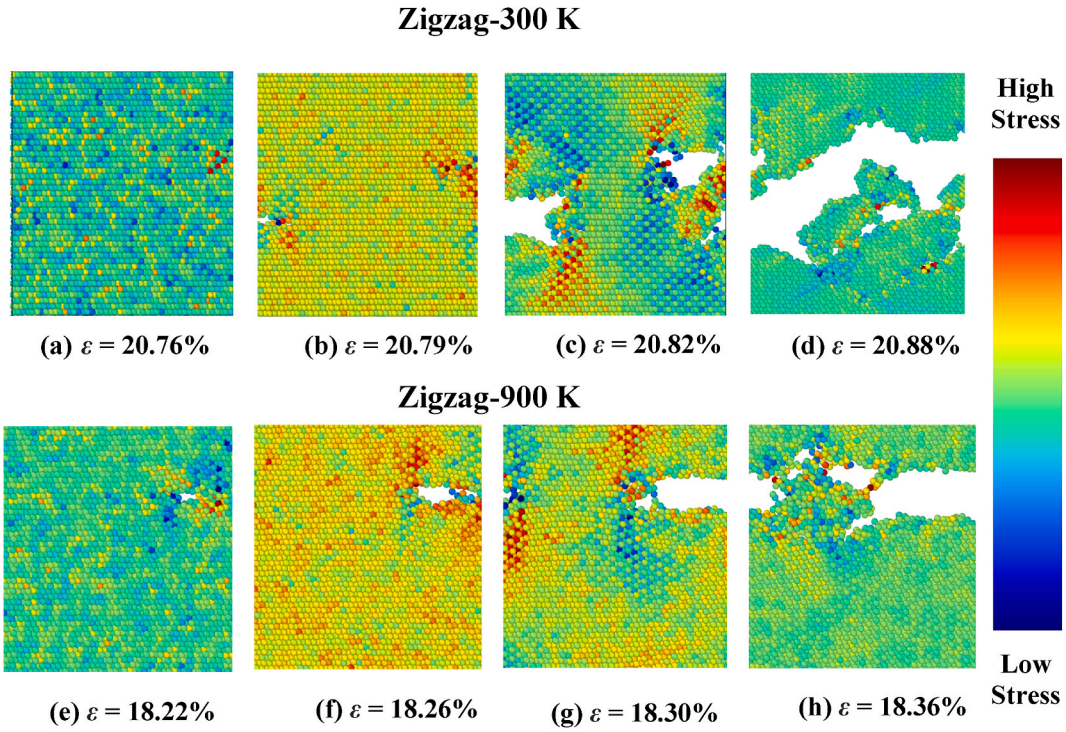

Fig. 6. Atomistic deformation profile of Ti_4C_3 nanosheets with increasing strain along zigzag direction at temperature of (a–d) 300 K, and (e–h) 900 K.

orientation-dependent anisotropic behavior of the Ti_4C_3 nanosheet is comparable with the previously studied 2D monolayers [22,27,31].

The current study examined the radial distribution function (RDF) at two distinct temperatures to further understand how temperature affects the mechanical behaviors of the Ti_4C_3 nanosheets. In Fig. 4(a–c), the partial radial distribution functions (RDFs) of the three nearest neighbors of the Ti_4C_3 structure, namely Ti-C, C-C, and Ti-Ti, are displayed. RDF at the temperature of 0 K should typically reflect delta-like functions. However, higher temperatures cause atoms to oscillate in and out, making it difficult to find a particular kind of atom at or around its ideal sites. Therefore, RDF shows a peak broadening and reduced peak intensities when the temperature increases. As displayed in Fig. 4(a–c), with the increase in temperature, RDF shows a gradual decrease in peak magnitude and widening of peaks for all of the nearest neighbors of Ti-Ti, C-C, and Ti-C. Observed peak positions for the first, second, and third nearest neighbors of Ti_4C_3 are 2.163, 3.066, and 3.0663 Å, respectively.

For a complete understanding of the impact of temperature, atomic level representation of the deformation profile is helpful. This study observed the atomistic fracture evolution at different temperatures for the simulated Ti_4C_3 nanosheet, including crack initiation, propagation, and rupturing. For simplicity, the fracture evolution profile at only 300 K and 900 K for armchair and zigzag loading, as illustrated in Figs. 5 and 6, respectively.

The patterns of all the deformation profiles are almost identical. The cracking initiation is observed at the stress-intensifying sites, usually at the edge or corner of the nanosheets. As the strain rises, the formed crack grows and quickly breaks down the nanosheets. Since all of these cracking initiations, propagations, and sample breaking take place fairly immediately (within a few ps), the Ti_4C_3 nanosheet exhibits brittle fracture phenomena. Figs. 5 and 6 show that cracking starts at 300 K when the strain is 26.26 % and 20.76 %, respectively, in the armchair and zigzag directions. However, when the temperature rises, cracking is observed to begin at lower values of applied strain. The equivalent values for 900 K are 17.80 % and 18.22 %, respectively, in the armchair and zigzag directions. This occurrence can be clarified because bond-rupturing occurs with greater frequency at elevated temperatures than at lower temperatures, which causes the nanosheets to break apart at higher temperatures despite lower strain values [30].

Another factor is the gradual growth of thermal vibration as temperature increases. The Ti_4C_3 system experiences extreme thermal trembling at 900 K. Thermal trembling causes atomic bonds to break and facilitates stress concentration at significantly reduced strain values. As a result, cracks are observed to appear inside the nanosheets at about 900 K, whereas free-edge acted as crack-initiating sites at 300 K. However, the cracking typically appears to propagate vertically to the direction of loading, which is comparable to the reported fracture phenomenon of different monolayers and 2D systems [34,52]. At the point of fracture strain, as found in the stress-strain illustration in Fig. 3(a and b), complete breaking of the nanosheet is precisely observed.

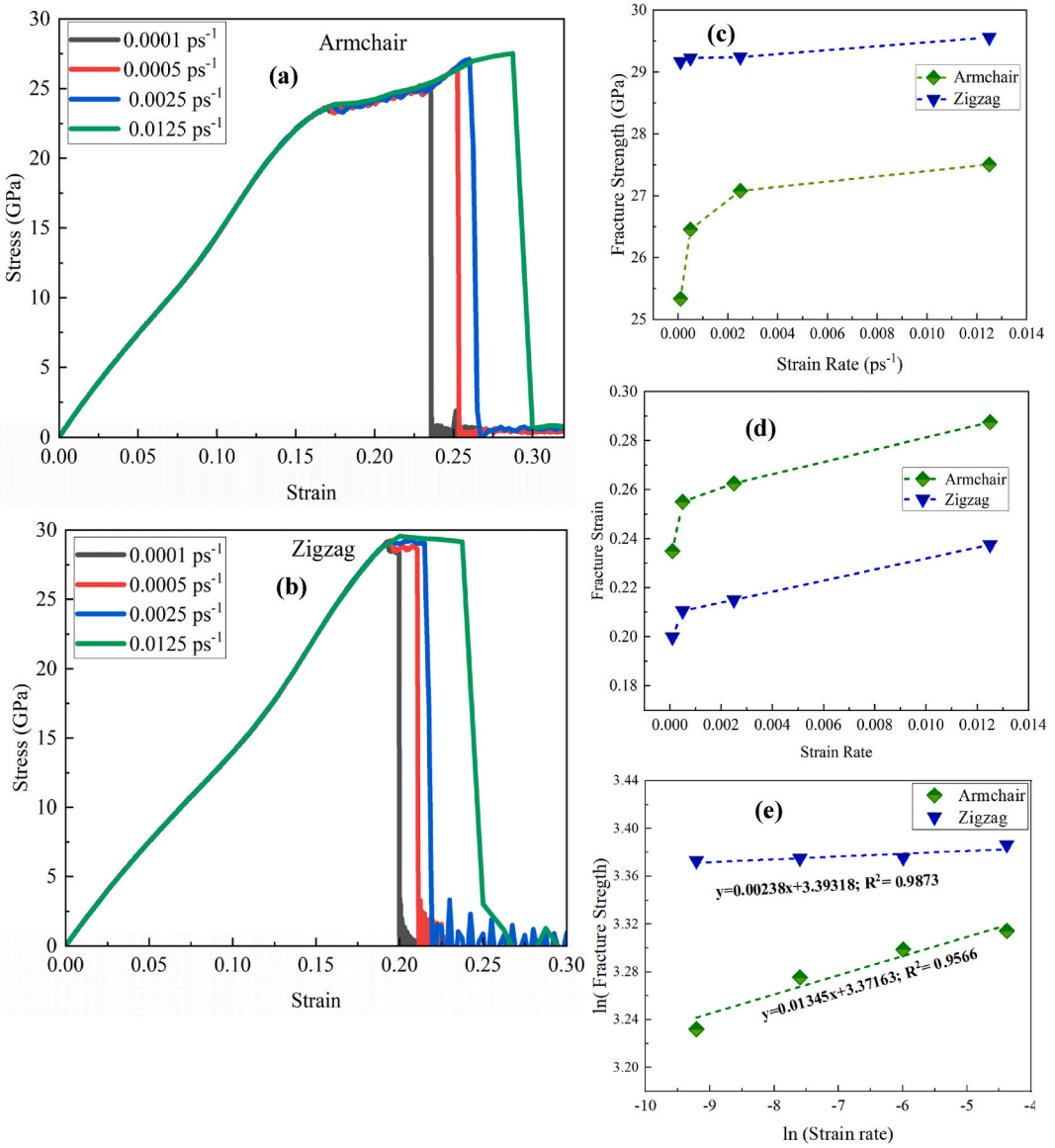

Fig. 7. Stress-strain diagram of Ti_4C_3 MXene depending on strain rates along (a) armchair and (b) zigzag directions. Strain rate dependent (c) fracture strength, (d) strain, and (e) strain rate sensitivity across directions.

3.3. Effect of strain rate

Li-ion battery electrode materials are subjected to many charging and discharging cycles throughout their lifetime. So, exploring the loading rate-dependent mechanical performance of anode material is of the utmost importance in developing safe and efficient LIBs [53]. This study examined the effects of strain rate on the tensile mechanical behavior of Ti_4C_3 MXene by subjecting the nanostructure to strain rates of 0.0001, 0.0005, 0.0025, and 0.0125 ps^{-1} at 300 K temperature throughout the entire simulation. The resulting stress-strain relationship across two chiral directions of the Ti_4C_3 sample at different strain rates is shown in Fig. 7(a, b). The initial sections of the curves in Fig. 7(a, b) coincide, indicating that the strain rate does not affect the elastic modulus of the structures in both directions. The effect of various strain rates on fracture strength and fracture strain is depicted in Fig. 7(c and d). As illustrated, the tensile strength and fracture strain both show an increased trend when the loading rate rises from 0.0001 ps^{-1} to 0.0125 ps^{-1} across directions. When a material undergoes loading at high speed, the stress and strain cannot be distributed identically throughout the entire volume; instead, they strike the rigid, substantial, and uncracked portion. As a result, with increasing loading rates, fracture strength and strain at failure exhibit an upward trend in both directions.

For the lowest loading rate of 0.0001 ps^{-1}, Ti_4C_3 nanosheets have the lowest tensile strength, measuring 25.33 GPa and 29.16 GPa across both directions. When strain rates increased from 0.0001 ps^{-1} to 0.0125 ps^{-1}, fracture strength increased by about 7.89 % and

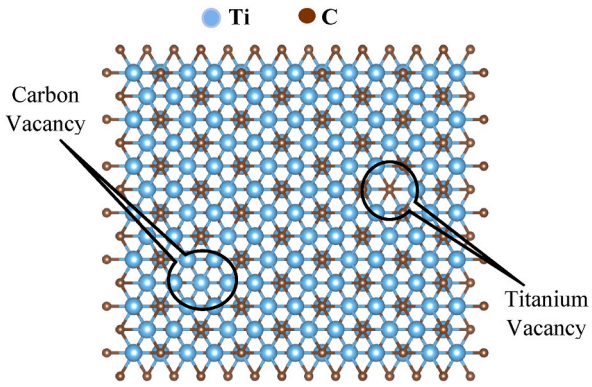

Fig. 8. Structural configuration of Ti_4C_3 with Titanium vacancy (TV) and Carbon vacancy (CV).

1.32 % in the armchair and zigzag direction, respectively, to reach 27.50 GPa and 29.55 GPa. Regardless of the applied strain rate, fracture strength along zigzag directions is higher than those along armchair directions. However, armchair-directed samples can withstand more significant failure strain than counter direction. Fracture strain in the armchair direction was 0.2356 when a minimum strain rate of 0.0001 ps^{-1} was applied, 15.19 % higher than the fracture strain along the counter direction of 0.1998. However, when the strain rate was raised to 0.0125 ps^{-1}, the fracture strain in the zigzag and armchair directions increased to 0.2875 and 0.2375. The corresponding percentage increments along the armchair and zigzag directions are approximately 18.05 and 15.87, respectively. The above analysis shows a significant impact of strain rate in the failure strain of Ti_4C_3 nanosheets, whereas the effect on fracture strength is not that significant. This significant strain rate impact on the mechanical performance of 2D Ti_4C_3 follows the reported data on previously studied 2D monolayers [26,54].

This study additionally explored the strain rate sensitivity, which is the variations in fracture strength of the sample as a linear function of the subjected loading rates, to investigate the strain rate sensitivity on the mechanical behavior of Ti_4C_3 MXenes. To determine the strain rate sensitivity, we employed Arrhenius' exponential relationship [55], which is represented as follows:

$$\dot{\epsilon} = A\sigma^{\frac{1}{m}} \exp\left(-\frac{Q}{RT}\right) \tag{9}$$

where,

$\dot{\varepsilon}$ = Applied loading rate
σ = Fracture strength
Q = Activation energy.
R = Universal gas constant.
T = Temperature in K scale
m = sensitivity of strain rate.
A = Arrhenius constant.

Eq. (9) becomes simpler if logarithms are used on both sides and temperature is set at a constant value since the simulation temperature was constant at 300 K. The Simplified equation is as follows:

$$\ln(\dot{\varepsilon}) = \ln(A) + \frac{1}{m}\ln(\sigma) - \frac{Q}{RT} \tag{10}$$

The slope of Eq. (10) can be denoted as strain rate sensitivity, as follows.

$$m = \frac{\partial \ln(\sigma)}{\partial \ln(\dot{\varepsilon})} \tag{11}$$

Fig. 7 (e) shows the logarithmic plot of the fracture strength with applied strain rates. From the plot, strain rate sensitivity in the armchair and zigzag directions are 0.01345 and 0.0238, respectively. So, the strain rate in the armchair loading is more sensitive than the zigzag loading. The atomic structure of the MXene, as shown in Fig. 1, can be utilized to clarify this characteristic. In each unit cell of the structure, four parallel bonds are present in the armchair direction, but none are in the contrary direction. Due to this configuration, the strain rate in the armchair direction has a more significant effect than the zigzag direction.

3.4. Effect of vacancy

It is practically impossible to synthesize crystal structures that are perfect or free of defects. Any experimentally produced crystalline 2D materials will unavoidably possess a variety of defects and imperfections. The most prominent and inevitable defect during the production and manufacturing of nanocrystals is point vacancy (PV) [30]. There are two possible kinds of point vacancies in Ti_4C_3 MXene: Ti (TV) and C vacancy (CV). The vacancy-induced Ti_4C_3 structure is demonstrated in Fig. 8, where carbon vacancy is created

Table 2
Potential energy per atom value for defect-free Ti_4C_3 structure; Ti and C vacancy formation energy of the MXene with the comparative plot of the previous study; % Diff = percent difference.

Parameters	This Study	DFT [43]	% Diff	MD (BOP) [43]	% Diff
PE/atom **(eV/atom)**	−6.87	−6.90	−0. 43 %	−6.79	1.18 %
E^f_{Ti1} **(eV)**	10.96	12.21	10.24 %	11.28	2.84 %
E^f_{C1} **(eV)**	8.82	9.47	6.86 %	9.55	7.64 %

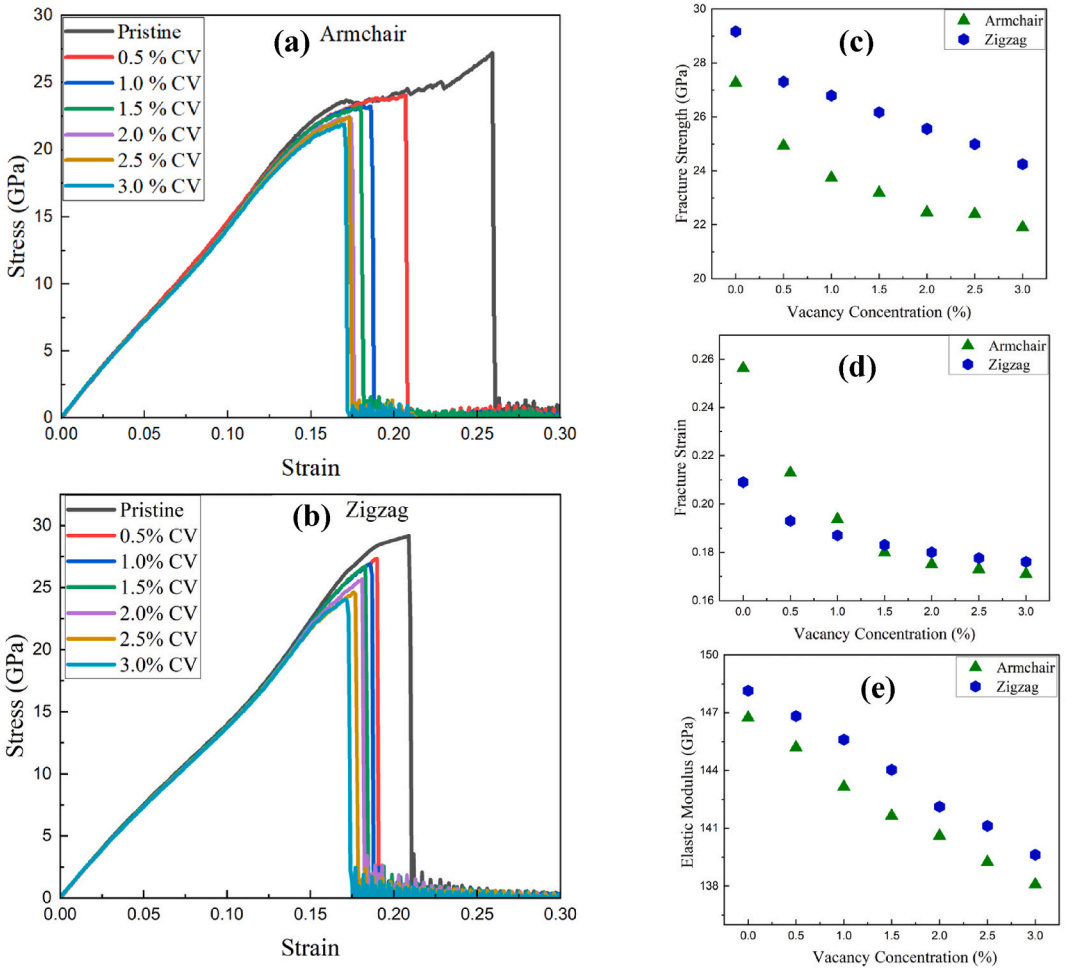

Fig. 9. Stress-strain diagram of Ti_4C_3 MXene depending on CV concentrations along the (a) armchair, and (b) zigzag orientations. Effect of carbon vacancy on (c) fracture strength, (d) strain, and (e) elasticity modulus.

by removing a carbon atom from the second layer, and titanium vacancy is made by removing an atom from the third layer. However, the vacancy-induced structure subjected to simulation in this study contains random vacant sites of respective atoms.

The energy required to facilitate the formation of a specific vacant site is a crucial component in determining the susceptibility of a material to point vacancies. Vacancy formation energy refers to the particular quantity of energy required to remove an individual atom from a perfect crystal. The vacancy-forming energies of these two types of vacancies were computed to better understand the likelihood of C- and Ti-vacancies occurring in Ti_4C_3 nanocrystals. The formation energy of a specific type of PV, denoted as E^f_v, is calculated in this work using the formula [56] as follows:

$$E^f_v = E_f - \left[\frac{(N_0 - 1)}{N_0}\right] \times E_i \tag{12}$$

Where,

E_i = Initial energy of defect-free Ti_4C_3 sample

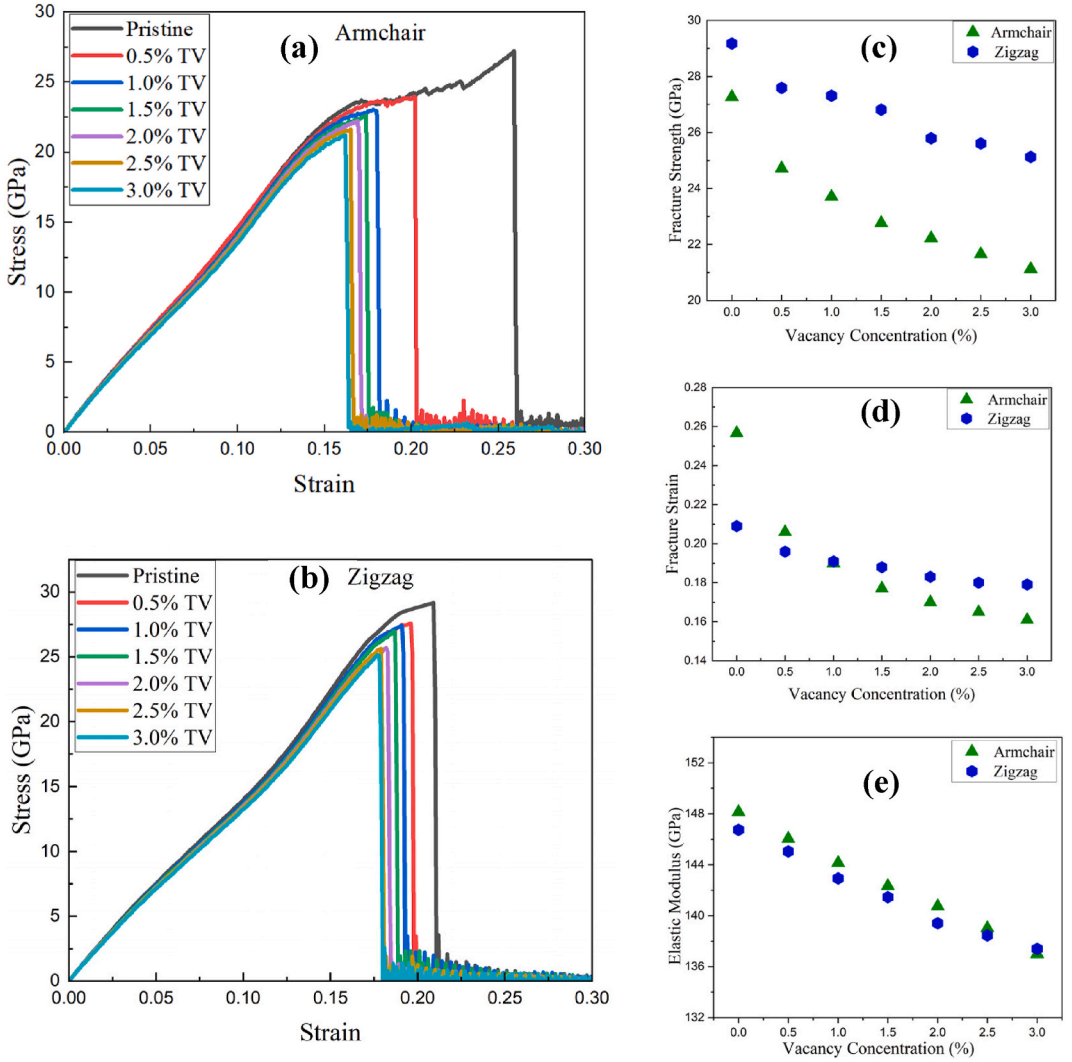

Fig. 10. Stress-strain diagram of Ti_4C_3 MXene depending on TV concentrations along the (a) armchair, and (b) zigzag orientations. Effect of titanium vacancy on (c) fracture strength, (d) strain, and (e) elasticity modulus.

E_f = Final energy after vacancy created

N_0 = Number of atoms in a defect-free sample

Table 2 shows this study's calculated values of the Ti and C vacancy formation energy and previously reported corresponding values using DFT and MD employing self-developed bond order potential [43]. We calculated formation energy for Ti-vacancy and C-vacancy, removing the corresponding atom from the third and fourth layer, respectively, and obtained values of 10.96 eV and 8.82 eV, respectively. Carbon point vacancy has lesser formation energy, meaning it is more probable to form inside the Ti_4C_3 structure, which agrees well with previously explored data [43].

This study meticulously explored the influence of CV and TV on the tensile mechanical behavior of Ti_4C_3 MXene. Temperature and strain rate were kept constant at 300 K and 0.001 ps^{-1}, respectively, while CV and TV's vacancy concentration varied up to 3 %. The stress-strain response of the Ti_4C_3 structure with induced carbon and titanium vacancy is shown in Fig. 9 (a, b) and Fig. 10 (a, b) for two loading directions. Corresponding stress-strain responses of pristine samples are also provided to easily comprehend the impact of both types of vacancies. All the stress-strain behavior has a remarkably comparable pattern in both directions. Each stress-strain curve begins out linearly, reflecting the sample's elastic features, and then abruptly breaks at the fracture strain point due to the brittle failure of the nanosheets. However, the strain-hardening tendency of armchair-oriented Ti_4C_3 structure is no longer observed in vacancy-induced samples. Extracted values of fracture strength, fracture strain, and elastic modulus of the vacancy-induced structure along two loading directions are illustrated in Fig. 9(c–e) and Fig. 10(c–e). The Young's modulus was determined using the whole elastic area up to the yield point. It is evident from the illustration that all of the fracture strength, fracture strain, and Young's modulus are in a downward trend with increasing CV and TV concentration.

The fracture strength of pristine Ti_4C_3 MXene was previously determined as 27.27 GPa and 29.17 GPa, respectively, in armchair

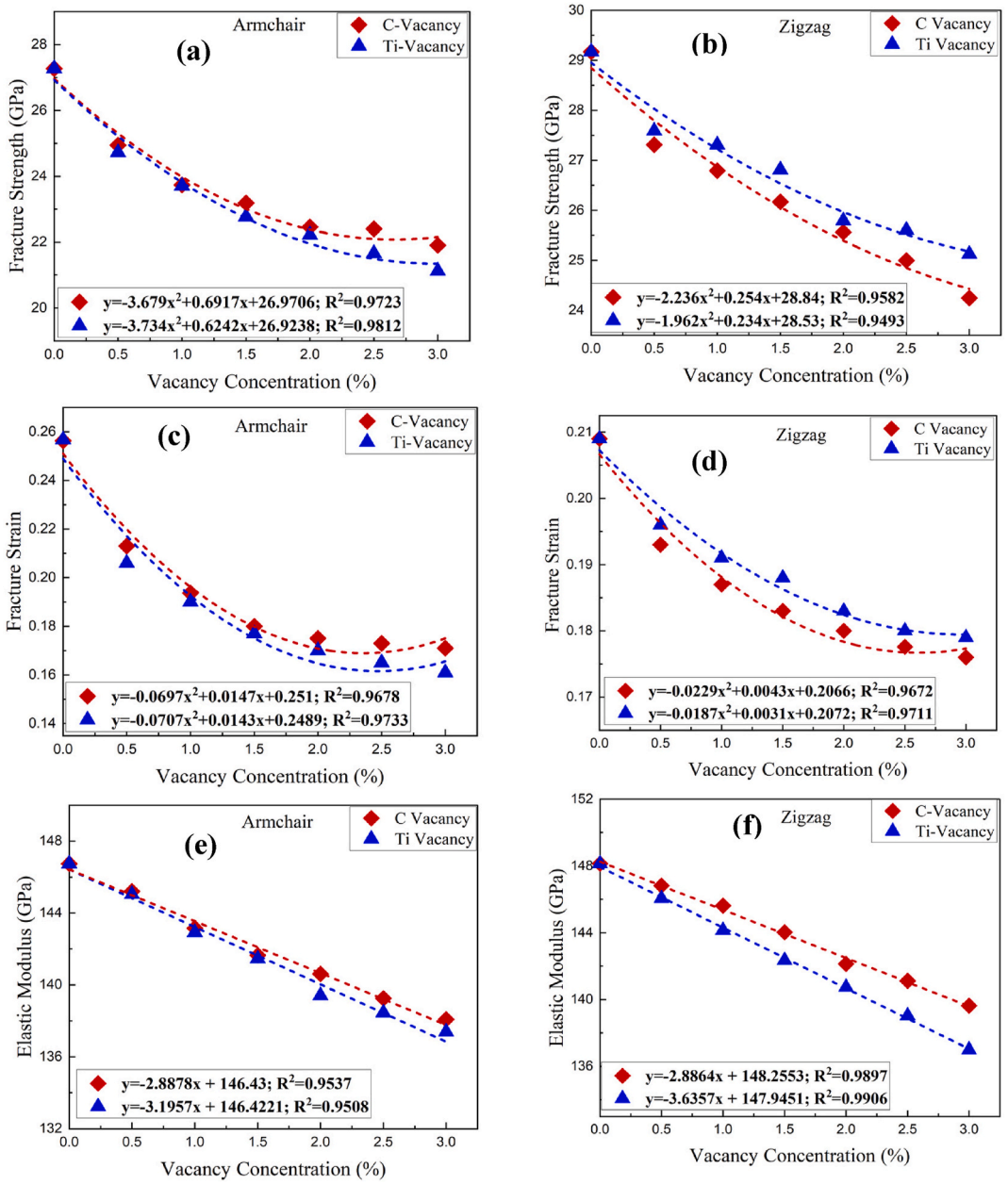

Fig. 11. Linear fit of the resulted (a, b) fracture strength, (c, d) strain, and (e, f) modulus of elasticity in point vacancy-induced Ti_4C_3 MXene along two loading directions.

and zigzag direction. These values decrease significantly with increasing vacancy concentrations of each type. Along armchair direction, fracture strength reduced at about 19.69 % and 22.55 %, respectively, in 3 % CV and TV-induced samples, to reach 21.9 GPa and 21.12 GPa, respectively. Along the zigzag direction, the estimated fracture strength of 3 % CV and TV-induced samples are 24.25 GPa and 25.12 GPa, respectively, with a corresponding decrement of 16.87 % and 13.88 % from the pristine sample. With increasing concentrations of CV and TV up to 3 %, fracture strain along both directions has also been found to be in decreasing order. Along the armchair direction, fracture strain decreases from the pristine sample's value of 0.259 to 0.171 and 0.161 for respective increases in concentrations of CV and TV. The corresponding decrements for CV and TV-induced samples are 33.89 % and 37.84 %, respectively.

On the contrary, the zigzag-oriented structure shows a decrement of 15.79 % and 14.35 % in fracture strain, as it drops from pristine samples value of 0.209 to 0.176 and 0.179, respectively, in 3 % of CV and TV. The significant drops in fracture strain value for the armchair-directed MXene sample can be comprehended from Figs. 9(a) and 10(a). It is apparent from the depiction that strain hardening tendency diminishes significantly with increasing vacancy concentrations of any type and is no longer observed beyond 0.5 % vacancy concentrations. As a result, fracture strain shows a significant drop in this direction.

In striking contrast to temperature and strain rate, both point vacancies have significantly influenced the elastic modulus of Ti_4C_3 MXene. It is also apparent from the stress-strain plot that the initial linear segments of the stress-strain diagram do not align precisely. The modulus of elasticity of the armchair-oriented MXene demonstrates a decrement of 5.90 % and 6.37 %, respectively, for the corresponding increase in CV and TV percentages from pristine state to 3 %. The elastic modulus of the pristine sample is 146.74 GPa in the armchair direction, which ended up at 138.08 GPa and 137.39 GPa, respectively, in 3 % carbon and titanium vacancy-induced samples. Contrarily, the elastic modulus in the zigzag orientations of the MXene drops from the pristine state's value of 148.14 GPa–139.6 GPa and 136.99 GPa, respectively, for the increase in carbon and titanium vacancy percentages up to 3 %. In percentage, the corresponding drops along the zigzag direction are measured as 5.76 and 7.53, with respective increases in CV and TV concentrations.

To compare the corresponding impact of each vacancy type, extracted tensile strength, fracture strain, and modulus of elasticity values resulting from these two vacancy-induced samples were plotted in the same curve with corresponding values of the pristine sample. The linear and polynomial fitted illustration in Fig. 11 makes it simple to comprehend how CV and TV have different impacts on the mechanical characteristics of Ti_4C_3 MXene in both directions. From the illustration in Fig. 11, fracture strength and fracture strain are fitted as a quadratic function of vacancy concentration, whereas elastic modulus is expressed as a linear function. The fracture strength and strain values decrease significantly in 0.5 % of vacant samples compared to the value of pristine samples. When vacancy concentrations increase further, the corresponding decrements are insignificant and follow an almost linear trend. This non-linear trend of vacancy-dependent fracture strength and fracture strain was reportedly observed in monolayer h-BCN [57]. Due to this non-linearity, quadratic polynomial expressions were required to depict the overall changes in fracture strength and fracture strain as a function of vacancy percentage. On the other hand, the elastic modulus of the samples was found to follow a linear function of vacancy concentrations, as previously reported in Ti_2C MXene [50].

As shown in Fig. 11(a and b), the changes in fracture strength of the Ti_4C_3 MXene as a function of vacancy concentrations can be expressed as follows:

Along armchair direction,

$$\sigma_f = -3.679x^2 + 0.6917x + 26.9706;\ R^2 = 0.9723\ [\text{where } x = \text{CV\%}] \tag{13}$$

$$\sigma_f = -3.734x^2 + 0.6242x + 26.9238;\ R^2 = 0.9812\ [\text{where } x = \text{TV\%}] \tag{14}$$

Along zigzag direction,

$$\sigma_f = -2.236x^2 + 0.254x + 28.84;\ R^2 = 0.9582\ [\text{where } x = \text{CV\%}] \tag{15}$$

$$\sigma_f = -1.962x^2 + 0.234x + 28.53;\ R^2 = 0.949\ [\text{where } x = \text{TV\%}] \tag{16}$$

From Eqs. 13–16, it is evident that titanium vacancy has a more impactful role in armchair loading, whereas carbon vacancy has a greater impact on fracture strength in zigzag loading.

Fracture strain also shows a similar decreasing trend, which is evident from the quadratic correlation of the fracture strain as a function of vacancy concentration, as illustrated in Fig. 11(c and d). It is observed from the correlation that titanium vacancy in the armchair direction and carbon vacancy in the zigzag direction have a comparatively more significant impact on fracture strain than their corresponding counter types. As shown in Fig. 1, carbon takes part in each ups and downs along the zigzag direction, being more critical than titanium, symmetry breakdown due to induced vacant carbon sites causes more damage in fracture strength and strain along this direction.

The linear fitted plot of elasticity modulus in Fig. 11 (e, f) reflects the detrimental impact of point vacancies on the elastic modulus of Ti_4C_3 MXene. The corresponding relation between elastic modulus and vacancy concentrations can be written as:

Along armchair direction:

$$E = -2.8878x + 146.43;\ R^2 = 0.9537\ [\text{where } x = \text{CV\%}] \tag{17}$$

$$E = -3.1957x + 146.4221;\ R^2 = 0.9508\ [\text{where } x = \text{TV\%}] \tag{18}$$

Along zigzag direction:

$$E = -2.8864x + 148.2553;\ R^2 = 0.9897\ [\text{where } x = \text{CV\%}] \tag{19}$$

$$E = -3.6357x + 147.9451;\ R^2 = 0.9906\ [\text{where } x = \text{TV\%}] \tag{20}$$

Carbon vacancy has been observed to show lesser impact along both directions with corresponding slopes of −2.8878 and −2.8864, respectively, in armchair and zigzag loading directions. Contrarily, titanium vacancy is observed to cause more impactful deterioration of elastic modulus, which is evident from its greater slope of −3.1957 and −3.6357, respectively, in the armchair and zigzag orientations.

Previous investigations on 2D materials showed that cohesive energy, also known as potential energy per atom (PE/atom), is a reliable measure of defective materials' alterations in mechanical functionality [44,58]. In order to understand the influence of point vacancies on the mechanical behavior of the Ti_4C_3 structure in a qualitative way, the potential energy for each atom (PE/atom) has been computed in this study. An ideal pristine crystal should have the least PE/atom value at the lowest strain value. However, the

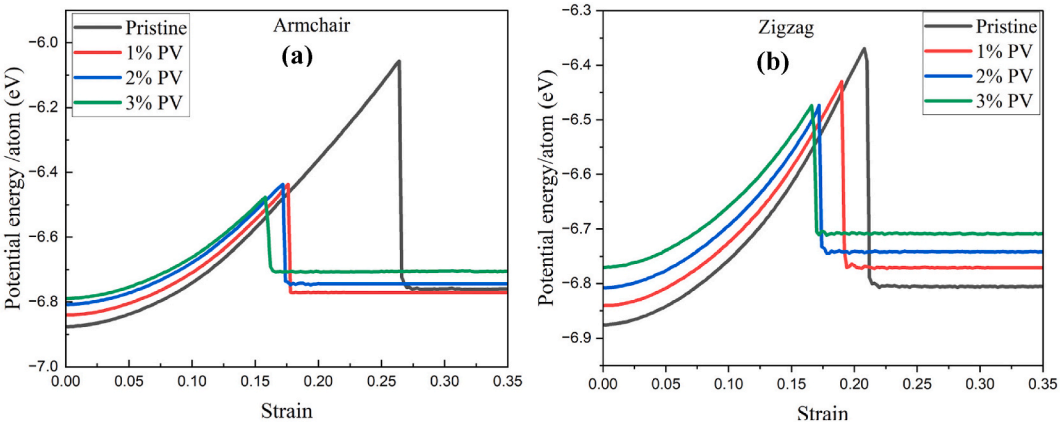

Fig. 12. Calculated values of Potential energy for each atom in pristine and random point-vacancy induced sample in the (a) armchair chirality, and (c, d) zigzag chirality.

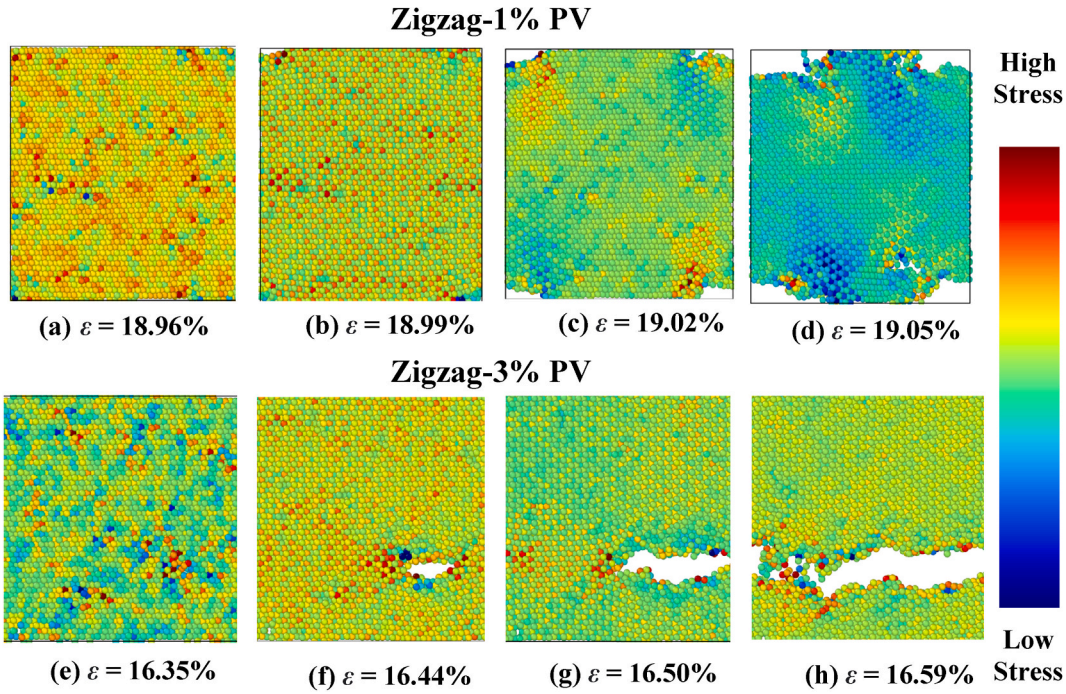

Fig. 13. Atomistic deformation profile of Ti_4C_3 nanosheets with increasing strain along zigzag direction for (a–d) 1 % of PV, and (e–h) 3 % of PV concentration.

value increases as the defect concentration in the crystal rises. This rise in potential energy is accelerated by the robust regularity failure effect caused by the induced vacancies. We have computed PE/atom for a random point vacancy-induced Ti_4C_3 structure along both loading orientations, which is shown in Fig. 12. As of the plot, the pristine sample shows minimum values of initial PE/atom than any of the vacancy-induced samples. According to the plot, the initial value is calculated as −6.87 eV/atom for the defect-free Ti_4C_3 crystal, which shows an excellent fit with that obtained from the previous study [43] However, the values increase due to increasing irregularities inside the structure with increasing vacancy concentrations. Apart from these, all the PE/atom plots show an identical pattern with a continuously increasing trend up to the fracture strain, followed by an abrupt drop as the nanosheet breakdown occurs.

In order to figure out the nature of the fracture, the atomistic deformation profile must be examined with increasing applied strain. This study also examined the impact of different vacancy concentrations on the atomistic deformation profile of the Ti_4C_3 nanosheets. The atomistic deformation profile for 1 % and 3 % of point vacancy-induced nanosheets along two loading directions are displayed in Figs. 13 and 14.

All the deformation profiles share similarities with the pristine state, except that point defects act as stress-rising sites here. It is

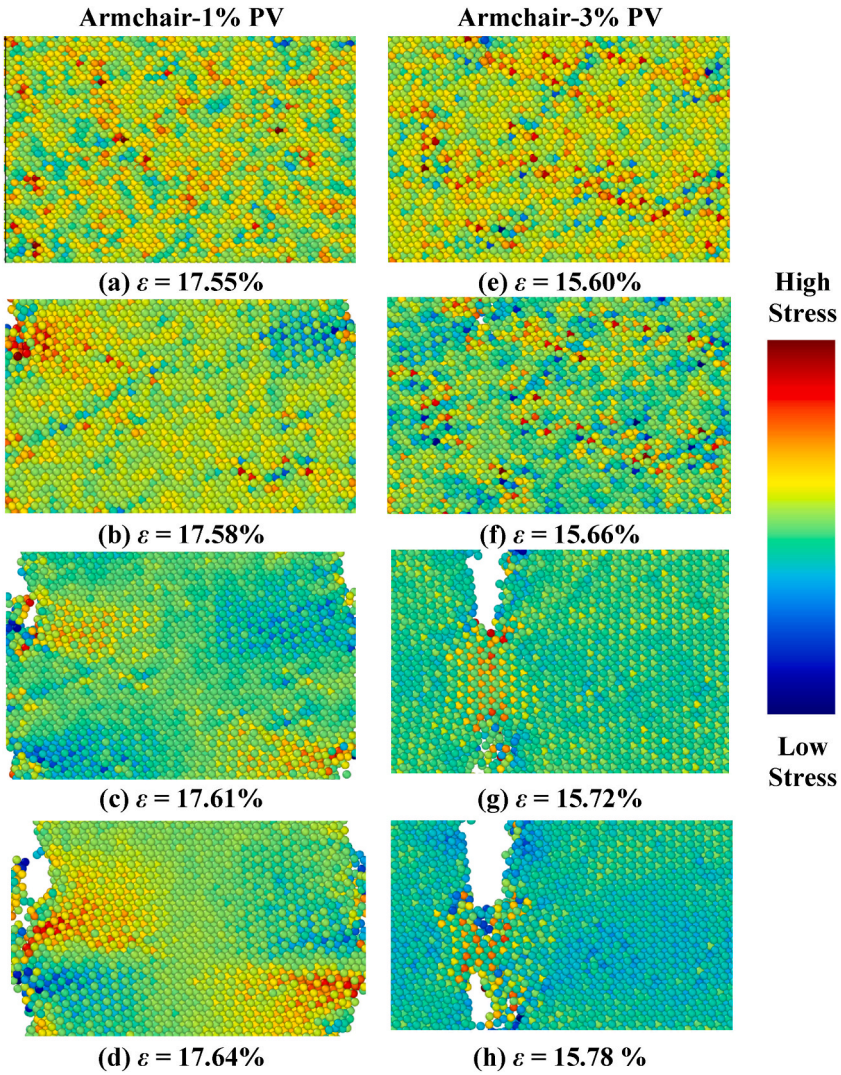

Fig. 14. Atomistic deformation profile of Ti_4C_3 nanosheets with increasing strain along armchair direction for (a–d) 1 % of PV, and (e–h) 3 % of PV concentration.

evident from the atomistic configurations that point vacancies acted as stress-intensifying sites and initiated cracks to form. In 1 % of point vacancy-induced nanosheets, cracks are observed to begin from the vacancies located at the corner of the sheet. In contrast, the initiation of cracks appears inside the nanosheets for 3 % of point vacancies. This is because 1 % of PV-induced samples do not have enough vacant sites to initiate cracks within the nanosheet, and 3 % of vacancy-induced samples contain sufficient vacant sites inside the structure. However, once a crack initiates, a considerable amount of stress concentration is apparent at the crack tip from the color coding, facilitating the crack to propagate and rupture the nanosheets quickly.

Another thing to observe is that rupturing of the nanosheets in the 1 % PV-induced sample does not necessarily take long (within 10–12 ps). In contrast, in the 3 % PV-induced sample, cracks propagating takes longer when crack initiates inside the structure. Nevertheless, all vacancy-induced nanosheets exhibit the exact brittle fracture mechanism as the pristine sample. Fracture strain value has also been found to decrease with increasing vacancy concentrations, supporting the data obtained from the stress-strain behavior of vacancy-induced Ti_4C_3 MXene.

4. Conclusion

In this study, we thoroughly investigated the tensile mechanical behavior and deformation profile of Ti_4C_3 MXene under different chiral directions, temperatures, strain rates, and vacancy concentrations using a classical molecular dynamics (MD) simulator, LAMMPS. Stress-strain behavior along two chiral orientations was utilized to determine the modulus of elasticity, tensile strength, and fracture strain of Ti_4C_3 MXene. At 300 K, the zigzag-directed Ti_4C_3 structure shows a slightly superior fracture strength and elastic

modulus than its counter direction. The fracture strength and elastic modulus values in the zigzag directions are 29.17 GPa and 148.14 GPa, respectively, which are 6.51 % and 0.81 % greater than its counter direction. Competitive elastic modulus and fracture stress data in the armchair and zigzag orientations confirm the insignificant anisotropy of Ti_4C_3 MXene. However, armchair-oriented Ti_4C_3 has been observed to possess a considerably greater fracture strain due to its strain-hardening tendency at lower temperatures. Fracture strain along the armchair direction at 300 K has been measured to be 0.259, 19.31 % greater than its counter direction. Temperature and strain rate cause opposite fracture strength and strain trend, whereas elastic modulus is nearly unaffected. Increasing temperature shows the most significant impact on fracture strain along armchair direction since the strain hardening tendency diminishes with increasing temperature and does not occur beyond 500 K. Obtained RDF data at different temperatures show a decrease in peak intensity and peak broadening at elevated temperature. From the slope of the logarithmic plot of the fracture strength-strain rate, armchair-oriented Ti_4C_3 is more sensitive to the applied strain rate than zigzag-oriented. Carbon vacancy possesses less formation energy than titanium, indicating it is more likely to form in the Ti_4C_3 structure. Potential energy per atom calculations also made the influence of point vacancies more understandable. Atomistic deformation profiles support the findings from stress-strain behavior and help to gain an improved comprehension of fracture phenomena. This deformation profile also made apparent the effect of thermal trembling at elevated temperatures and the tendency of vacancies to act as stress-intensifying sites. This comprehensive study provided detailed mechanical behavior and fracture phenomena of Ti_4C_3 MXene under various environmental circumstances. This will facilitate its employment in the safe and efficient designing of anode materials for Li-ion batteries.

Data availability

The corresponding authors can provide the data required to reproduce these findings upon reasonable request.

CRediT authorship contribution statement

Wahidur Rahman Sajal: Writing – original draft, Validation, Software, Methodology, Formal analysis, Conceptualization. **Md. Mehidi Hassan:** Writing – original draft, Visualization, Validation, Software, Methodology, Data curation. **Jahirul Islam:** Writing – review & editing, Validation, Supervision, Software, Methodology, Conceptualization. **Tipu Sultan:** Writing – review & editing, Resources. **Md. Bokhtiar Hossen:** Visualization, Software. **Abdullah Arafat:** Writing – review & editing, Data curation.

Declaration of competing interest

The authors declare that they have no known competing financial interests or personal relationships that could have appeared to influence the work reported in this paper.

Acknowledgments

The research was conducted at the Computational Materials Science Laboratory in the Department of Materials Science and Engineering at Khulna University of Engineering & Technology, Khulna 9203, Bangladesh.

References

[1] S. Chu, A. Majumdar, Opportunities and challenges for a sustainable energy future, Nature (2012), https://doi.org/10.1038/nature11475.
[2] Y. Liang, C.Z. Zhao, H. Yuan, et al., A review of rechargeable batteries for portable electronic devices, InfoMat (2019), https://doi.org/10.1002/inf2.12000.
[3] A.L.M. Reddy, S.R. Gowda, M.M. Shaijumon, P.M. Ajayan, Hybrid nanostructures for energy storage applications, Adv. Mater. (2012), https://doi.org/10.1002/adma.201104502.
[4] J.M. Tarascon, M. Armand, Issues and challenges facing rechargeable lithium batteries, Nature (2001), https://doi.org/10.1038/35104644.
[5] M. Winter, J.O. Besenhard, M.E. Spahr, P. Novák, Insertion electrode materials for rechargeable lithium batteries, Adv. Mater. (1998), https://doi.org/10.1002/(SICI)1521-4095(199807)10:10<725::AID-ADMA725>3.0.CO;2-Z.
[6] N.K. Chaudhari, H. Jin, B. Kim, D. San Baek, S.H. Joo, K. Lee, Correction: MXene: an emerging two-dimensional material for future energy conversion and storage applications, J Mater Chem A Mater (2018), https://doi.org/10.1039/c7ta90287e.
[7] M. Zhang, R. Hu, J. Liu, L. Ouyang, Jun liu, L. Yang, F. Fang, M. Zhu, AgP2/C as an anode for high rate performance lithium-ion batteries, J. Alloys Compd. (2018), https://doi.org/10.1016/j.jallcom.2018.05.244.
[8] H. Zhang, Z. Fu, R. Zhang, Q. Zhang, H. Tian, D. Legut, T.C. Germann, Y. Guo, S. Du, J.S. Francisco, Designing flexible 2D transition metal carbides with strain-controllable lithium storage, Proc Natl Acad Sci U S A (2017), https://doi.org/10.1073/pnas.1717219115.
[9] T. Stephenson, Z. Li, B. Olsen, D. Mitlin, Lithium ion battery applications of molybdenum disulfide (MoS2) nanocomposites, Energy Environ. Sci. (2014), https://doi.org/10.1039/c3ee42591f.
[10] Y. Jing, Z. Zhou, C.R. Cabrera, Z. Chen, Graphene, inorganic graphene analogs and their composites for lithium ion batteries, J Mater Chem A Mater (2014), https://doi.org/10.1039/c4ta01033g.
[11] K. Toyoura, Y. Koyama, A. Kuwabara, I. Tanaka, Effects of off-stoichiometry of LiC6 on the lithium diffusion mechanism and diffusivity by first principles calculations, J. Phys. Chem. C (2010), https://doi.org/10.1021/jp910134u.
[12] G. Gao, A.P. O'Mullane, A. Du, 2D MXenes: a new family of promising catalysts for the hydrogen evolution reaction, ACS Catal. (2017), https://doi.org/10.1021/acscatal.6b02754.
[13] M. Naguib, V.N. Mochalin, M.W. Barsoum, Y. Gogotsi, 25th anniversary article: MXenes: a new family of two-dimensional materials, Adv. Mater. (2014), https://doi.org/10.1002/adma.201304138.
[14] P. Kumar, S. Singh, S.A.R. Hashmi, K.H. Kim, MXenes: emerging 2D materials for hydrogen storage, Nano Energy (2021), https://doi.org/10.1016/j.nanoen.2021.105989.
[15] O. Salim, K.A. Mahmoud, K.K. Pant, R.K. Joshi, Introduction to MXenes: synthesis and characteristics, Mater. Today Chem. (2019), https://doi.org/10.1016/j.mtchem.2019.08.010.

[16] M. Naguib, J. Halim, J. Lu, K.M. Cook, L. Hultman, Y. Gogotsi, M.W. Barsoum, New two-dimensional niobium and vanadium carbides as promising materials for li-ion batteries, J. Am. Chem. Soc. (2013), https://doi.org/10.1021/ja405735d.

[17] C.E. Ren, M.Q. Zhao, T. Makaryan, J. Halim, M. Boota, S. Kota, B. Anasori, M.W. Barsoum, Y. Gogotsi, Porous two-dimensional transition metal carbide (MXene) flakes for high-performance Li-ion storage, Chemelectrochem (2016), https://doi.org/10.1002/celc.201600059.

[18] M. Naguib, J. Come, B. Dyatkin, V. Presser, P.L. Taberna, P. Simon, M.W. Barsoum, Y. Gogotsi, MXene: a promising transition metal carbide anode for lithium-ion batteries, Electrochem. Commun. (2012), https://doi.org/10.1016/j.elecom.2012.01.002.

[19] Y. Xie, Y. Dall'Agnese, M. Naguib, Y. Gogotsi, M.W. Barsoum, H.L. Zhuang, P.R.C. Kent, Prediction and characterization of mxene nanosheet anodes for non-lithium-ion batteries, ACS Nano (2014), https://doi.org/10.1021/nn503921j.

[20] D. Er, J. Li, M. Naguib, Y. Gogotsi, V.B. Shenoy, Ti3C2 MXene as a high capacity electrode material for metal (Li, Na, K, Ca) ion batteries, ACS Appl. Mater. Interfaces (2014), https://doi.org/10.1021/am501144q.

[21] V.N. Borysiuk, V.N. Mochalin, Y. Gogotsi, Bending rigidity of two-dimensional titanium carbide (MXene) nanoribbons: a molecular dynamics study, Comput. Mater. Sci. (2018), https://doi.org/10.1016/j.commatsci.2017.11.028.

[22] M. Kurtoglu, M. Naguib, Y. Gogotsi, M.W. Barsoum, First principles study of two-dimensional early transition metal carbides, MRS Commun (2012), https://doi.org/10.1557/mrc.2012.25.

[23] S.M. Hatam-Lee, A. Esfandiar, A. Rajabpour, Mechanical behaviors of titanium nitride and carbide MXenes: a molecular dynamics study, Appl. Surf. Sci. (2021), https://doi.org/10.1016/j.apsusc.2021.150633.

[24] T. Liang, T.R. Shan, Y.T. Cheng, B.D. Devine, M. Noordhoek, Y. Li, Z. Lu, S.R. Phillpot, S.B. Sinnott, Classical atomistic simulations of surfaces and heterogeneous interfaces with the charge-optimized many body (COMB) potentials, Mater. Sci. Eng. R Rep. (2013), https://doi.org/10.1016/j.mser.2013.07.001.

[25] Z. Huang, Y. Wang, M. Zhang, Theoretical investigations of Ti4C3 and Ti4C3T2 (T = F, O and OH) monolayers as anode materials for Li-ion batteries, FlatChem (2023), https://doi.org/10.1016/j.flatc.2023.100491.

[26] Y.Y. Zhang, Q.X. Pei, Y.W. Mai, Y.T. Gu, Temperature and strain-rate dependent fracture strength of graphynes, J. Phys. D Appl. Phys. (2014), https://doi.org/10.1088/0022-3727/47/42/425301.

[27] A.S.M.J. Islam, M.S. Islam, N. Ferdous, J. Park, A.G. Bhuiyan, A. Hashimoto, Anisotropic mechanical behavior of two dimensional silicon carbide: effect of temperature and vacancy defects, Mater. Res. Express (2019), https://doi.org/10.1088/2053-1591/ab5a96.

[28] Tipu Sultan, Jahirul Islam, Md Mehidi Hassan, Mechanical behaviors of the single crystal two-dimensional silicon carbide (SiC): a molecular dynamics insight, Malaysian Journal on Composites Science and Manufacturing 12 (2023) 102–113.

[29] Z.D. Sha, Q.X. Pei, Z. Ding, J.W. Jiang, Y.W. Zhang, Mechanical properties and fracture behavior of single-layer phosphorene at finite temperatures, J. Phys. D Appl. Phys. (2015), https://doi.org/10.1088/0022-3727/48/39/395303.

[30] A.S.M.J. Islam, M.S. Akbar, M.S. Islam, J. Park, Temperature- and defect-induced uniaxial tensile mechanical behaviors and the fracture mechanism of two-dimensional silicon germanide, ACS Omega (2021), https://doi.org/10.1021/acsomega.1c01691.

[31] R. Paul, T. Tasnim, S. Saha, M. Motalab, Atomistic analysis to characterize the impact of temperature and defects on the mechanical properties of germanene sheet, Mater. Res. Express (2018), https://doi.org/10.1088/2053-1591/aaa73d.

[32] G.A. Tritsaris, M.G. Åžensoy, S.N. Shirodkar, E. Kaxiras, First-principles study of coupled effect of ripplocations and S-vacancies in MoS2, J. Appl. Phys. (2019), https://doi.org/10.1063/1.5099496.

[33] M.S. Islam, S. Tanaka, A. Hashimoto, Effect of vacancy defects on phonon properties of hydrogen passivated graphene nanoribbons, Carbon N Y (2014), https://doi.org/10.1016/j.carbon.2014.08.049.

[34] A. Mahata, J.W. Jiang, D.R. Mahapatra, T. Rabczuk, Effect of intrinsic structural defects on mechanical properties of single layer MoS 2, Nano-Structures and Nano-Objects (2019), https://doi.org/10.1016/j.nanoso.2019.01.006.

[35] M.M. Hassan, J. Islam, W.R. Sajal, M.A.A.B. Shuvo, S. Goni, Temperature, strain rate, and point vacancy dependent anisotropic mechanical behaviors of titanium carbide (Ti3C2) MXene: a molecular dynamics study, Mater. Today Commun. (2023), https://doi.org/10.1016/j.mtcomm.2023.106898.

[36] A.P. Thompson, H.M. Aktulga, R. Berger, et al., Lammps - a flexible simulation tool for particle-based materials modeling at the atomic, meso, and continuum scales, Comput. Phys. Commun. (2022), https://doi.org/10.1016/j.cpc.2021.108171.

[37] I.R. Shein, A.L. Ivanovskii, Graphene-like titanium carbides and nitrides Ti n+1C n, Ti n+1N n (n = 1, 2, and 3) from de-intercalated MAX phases: first-principles probing of their structural, electronic properties and relative stability, Comput. Mater. Sci. (2012), https://doi.org/10.1016/j.commatsci.2012.07.011.

[38] M. Naguib, M. Kurtoglu, V. Presser, J. Lu, J. Niu, M. Heon, L. Hultman, Y. Gogotsi, M.W. Barsoum, Two-dimensional nanocrystals: two-dimensional nanocrystals produced by exfoliation of Ti3AlC2, Adv. Mater. 37/2011). Advanced Materials (2011), https://doi.org/10.1002/adma.201190147.

[39] J. Wang, J. Wang, Y. Zhou, Stable M2AlC(0001) surfaces (M = Ti, v and Cr) by first-principles investigation, J. Phys. Condens. Matter (2008), https://doi.org/10.1088/0953-8984/20/22/225006.

[40] L. Patra, R. Pandey, Mechanical properties of 2D materials: a review on molecular dynamics based nanoindentation simulations, Mater. Today Commun. (2022), https://doi.org/10.1016/j.mtcomm.2022.103623.

[41] Y.Y. Zhang, Q.X. Pei, Z.D. Sha, Y.W. Zhang, A molecular dynamics study of the mechanical properties of h-BCN monolayer using a modified Tersoff interatomic potential, Physics Letters, Section A: General, Atomic and Solid State Physics (2019), https://doi.org/10.1016/j.physleta.2019.05.055.

[42] G. Plummer, G.J. Tucker, Bond-order potentials for the Ti3AlC2 and Ti3SiC2 MAX phases, Phys. Rev. B (2019), https://doi.org/10.1103/PhysRevB.100.214114.

[43] G. Plummer, S. Thomas, M. Asle Zaeem, G.J. Tucker, Bond-order potential for the surface-terminated titanium carbide MXene monolayers Tin+1 CnTx (n=1,2, or 3;T=- O or - F), Phys Rev B (2022), https://doi.org/10.1103/PhysRevB.106.054105.

[44] Q. Lu, W. Gao, R. Huang, Atomistic simulation and continuum modeling of graphene nanoribbons under uniaxial tension, Model Simul Mat Sci Eng (2011), https://doi.org/10.1088/0965-0393/19/5/054006.

[45] R. Grantab, V.B. Shenoy, R.S. Ruoff, Anomalous strength characteristics of tilt grain boundaries in graphene, Science (2010), https://doi.org/10.1126/science.1196893, 1979.

[46] D.H. Tsai, The virial theorem and stress calculation in molecular dynamics, J. Chem. Phys. (1979), https://doi.org/10.1063/1.437577.

[47] A. Stukowski, Visualization and analysis of atomistic simulation data with OVITO-the Open Visualization Tool, Model Simul Mat Sci Eng. (2010), https://doi.org/10.1088/0965-0393/18/1/015012.

[48] S. Ma, M. Jiang, P. Tao, C. Song, J. Wu, J. Wang, T. Deng, W. Shang, Temperature effect and thermal impact in lithium-ion batteries: a review, Prog. Nat. Sci.: Mater. Int. (2018), https://doi.org/10.1016/j.pnsc.2018.11.002.

[49] N. Zhang, T. Deng, S. Zhang, C. Wang, L. Chen, C. Wang, X. Fan, Critical review on low-temperature Li-Ion/Metal batteries, Adv. Mater. (2022), https://doi.org/10.1002/adma.202107899.

[50] M.M. Hassan, J. Islam, W.R. Sajal, M.N.H. Noman, M.A. Rahman, Atomistic simulation of the mechanical behaviors of the pristine and vacancy-induced Ti2C MXene: effect of temperature, strain rate, and chirality, Heliyon 10 (2024) e25913.

[51] S. Thomas, K.M. Ajith, M.C. Valsakumar, Empirical potential influence and effect of temperature on the mechanical properties of pristine and defective hexagonal boron nitride, Mater. Res. Express (2017), https://doi.org/10.1088/2053-1591/aa72bf.

[52] B. Mortazavi, S. Ahzi, Thermal conductivity and tensile response of defective graphene: a molecular dynamics study, Carbon N Y (2013), https://doi.org/10.1016/j.carbon.2013.07.017.

[53] A. Sonwane, C. Yuan, J. Xu, Coupling effect of state-of-charge and strain rate on the mechanical behavior of electrodes of 21700 lithium-ion battery, Journal of Electrochemical Energy Conversion and Storage (2021), https://doi.org/10.1115/1.4049042.

[54] N. Li, N. Ding, S. Qu, L. Liu, W. Guo, C.M.L. Wu, Mechanical properties and failure behavior of hexagonal boron nitride sheets with nano-cracks, Comput. Mater. Sci. (2017), https://doi.org/10.1016/j.commatsci.2017.09.011.

[55] X. Wang, Y. Hong, M. Wang, G. Xin, Y. Yue, J. Zhang, Mechanical properties of molybdenum diselenide revealed by molecular dynamics simulation and support vector machine, Phys. Chem. Chem. Phys. (2019), https://doi.org/10.1039/c8cp07881e.

[56] S. Das, S. Mojumder, T. Rakib, M.M. Islam, M. Motalab, Atomistic insights into mechanical and thermal properties of stanene with defects, Physica B Condens Matter (2019), https://doi.org/10.1016/j.physb.2018.10.035.
[57] Y.Y. Zhang, Q.X. Pei, Z.D. Sha, Y.W. Zhang, A molecular dynamics study of the mechanical properties of h-BCN monolayer using a modified Tersoff interatomic potential, Phys. Lett. 383 (2019) 2821–2827.
[58] Y.J. Sun, Y.H. Huang, F. Ma, D.Y. Ma, T.W. Hu, K.W. Xu, Molecular dynamics simulation on double-elastic deformation of zigzag graphene nanoribbons at low temperature, Mater Sci Eng B Solid State Mater Adv Technol (2014), https://doi.org/10.1016/j.mseb.2013.10.00459.